Theoretical and Experimental Investigation on Body Control after Perching for Flapping-Wing Robots: Extending the Workspace for Manipulation

Pablo Serrano Luque, Alvaro C. Satue, Saeed Rafee Nekoo, Jose Angel Acosta, and Anibal Ollero

This work investigates a post-perching control for flapping-wing flying robots (FWFRs) to control and move the system on a branch. The flapping-wing aerial systems are lightweight platforms that mimic the birds' flight and they could serve for monitoring and inspection. The interaction of the FWFRs with the environment needs to fulfill perching on a branch, as a preliminary step, then moving the body to gain access to the desired pose and workspace. The leg of the robot moves the bird to the proper position. This work studies the mathematical modeling, simulation, and experimental implementation of this topic. A three-degree-of-freedom system is presented to model the robot's body, tail, and leg. A nonlinear controller, so-called feedback linearization (FL) is used for the control of the robot. A linear quadratic regulator (LQR), plus an integrator, are embedded in the FL controller to deliver optimal control for the linearized system. The simulation results show that the actuated leg extends the workspace of the robot significantly and confirms the effectiveness of the proposed strategy for body control. Experimental results present similar behavior of the system using the proposed controller for different desired setpoints.

***Index Terms*—Flapping-wing, Aerial robotics, Body control, Post-perching control.**

I. Introduction

THIS work investigates the stabilization and control of a flapping-wing flying robot (FWFR) after perching on a branch. A complete cycle of flight for a flapping-wing robot includes several phases. Firstly, the FWFR is shot by a launching system to gain the necessary initial speed. Then the robot performs a controlled flight towards a branch, which is the desired final condition of flight and perches on it. The controlled flight and perching on a branch were investigated in previous literature [1]; however, the correction of the posture and orientation of the body were not addressed. The orientation of the robot after perching might not be desirable for doing manipulation and the accessible workspace might not be proper. Hence, the leg of the FWFR should perform a controlled motion to change the posture of the robot while the claw holds the robot on the branch, please see Fig. 1 which shows an FWFR placed on a branch in indoor testbed; a two degree-of-freedom manipulator installed at the tip of the robot for manipulation of light objects. This work focuses on the controlled motion of the robot after perching. This topic has been investigated in the literature (with various scenarios and objectives) which is reviewed briefly here. Modeling and experimental study for a bird prototype with claw and manipulator were presented to consider the effect of motion of the arm and base on the center-of-mass (CoM) of the robot [2].

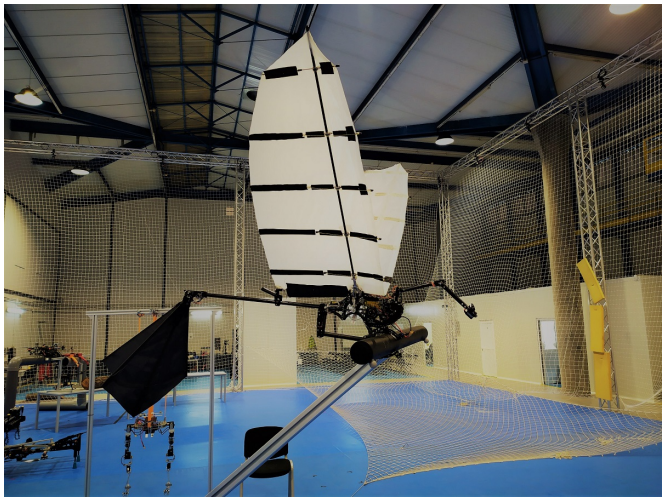

Fig. 1. The flapping-wing robot and manipulator on top, ready for pick-and-place task.

A nonlinear controller was designed for the system and the prototype was limited to stationary conditions and was not tested for flight. A controller that was aware of the limitation of a manipulator for a flapping-wing robot was presented to avoid the fall while the system was set on a branch [3]. The aerial system was imitating the bird's natural behavior and experimented with a stationary setup. This current work will simulate, experiment, and perform analysis on a flapping-wing model for having controlled motion on a branch after perching. The motivation for this motion control is to increase the workspace of the mounted manipulator on top of the bird. The manipulator was designed very lightweight with a 20cm reach, placed at the tip of the FWFR [4]. The motion of the robot will increase the workspace drastically, see Fig. 2.

The authors are with the GRVC Robotics Lab., Departamento de Ingeniería de Sistemas y Automática, Escuela Técnica Superior de Ingeniería, Universidad de Sevilla, Seville, Spain. E-mails: pabloserranoluque99@gmail.com, alvsatcre@alum.us.es, saerafee@yahoo.com, jaar@us.es, aollero@us.es.

This work was supported by the European Project GRIFFIN ERC Advanced Grant 2017, Action 788247; and partial support by PAIDI 2020 through the Project HOMPOT under Grant P20_00597.

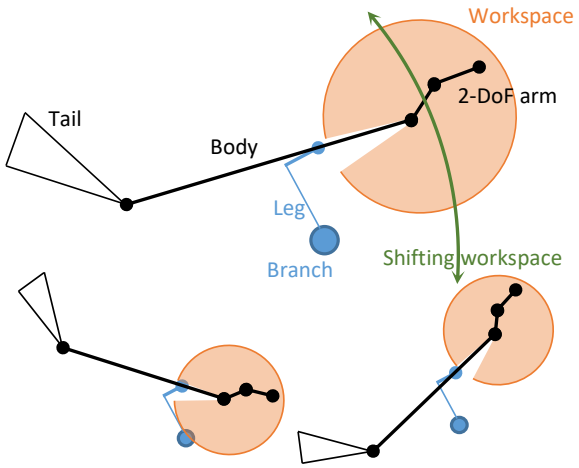

Fig. 2. The increased workspace of the flapping-wing robot using an active leg.

The perching topic is not limited to flapping-wing systems and it was explored with other aerial platforms as well. Roderick et al. presented a dual-leg design under a multirotor [5]. The multirotor provided a stable flight condition for the bio-inspired legs to demonstrate the perching capability of the system. Lin et al. used a gripper under an unmanned aerial vehicle (UAV) for perching on top of a round timber post [6]. Stewart et al. presented a passive claw-shape perching mechanism for a fixed-wing system that could perch up to 7(m/s) speed [7]. Another example of fixed-wing system was studied a method to swoop and grasp rapidly using a passive claw to perch like the birds [8]. Broers and Armanini presented a soft claw for perching, 45(g), installed under a multi-copter with perching experiments [9]. The energy efficiency was considered and a servomotor was selected for the actuation of the claw considering the minimization of battery usage.

The claw-shape mechanisms for the perching of "flapping-wing robots" are hardly reported (there are reports on bio-inspired claws installed under other platforms such as [5], [8], [9], but under the flapping-wing systems, rarely seen [1]). Gomez-Tamm et al. proposed a bio-inspired soft claw for flapping-wing robots considering the lightweight design and using shape memory alloy actuators [10]. The power grip and adaptation to the shape of the branch for perching or for holding an object were reported though the flight performance was not mentioned. This work uses a claw under the flapping-wing robot for holding the robot on a branch. The controlled flight of the FWFR was investigated for carrying the leg and manipulator simultaneously [4]. Here the flight and perch are not the focus, though the paper involves the motion control on a branch by the leg-claw subsystem.

The presented model for motion control of the body is a three-degree-of-freedom (DoF) linkage and is highly nonlinear. Feedback linearization (FL) is a well-known nonlinear method for controlling such systems, especially in robotics.

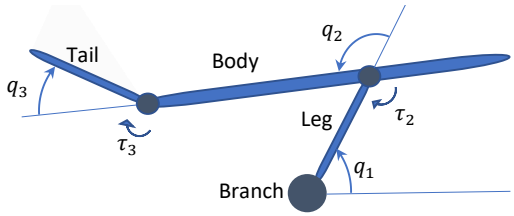

Fig. 3. The schematic and joint definition of the mathematical model of the FWFR.

Laubscher et al. presented a hybrid impedance sliding mode control for lower limb exoskeleton control of a biped system, in which feedback linearization was used for inner loops of control [11]. Zhang et al. investigated the control of wheeled mobile robots using a Lyapunov-stable feedback linearization approach [12]. Modification of the FL controllers is an important advantage of this method, i.e., a robust feedback linearization method was proposed for a robotic system [13]. The method was also implemented on a parallel cable-driven robot [14].

Combining optimal control with the FL method was introduced using various schemes to increase the performance and reduce the energy consumption in a trade-off. Martins et al. applied a nonlinear inner-loop FL control on a UAV and also employed LQR with integrative action in the outer and inner loop [15]. Application of the LQR design on the linearized dynamics of a cable-driven mobile robot was illustrated for increasing load-carrying capacity [16]. Here in this work, the same approach is used to provide an optimal trade-off between the error and input control using a linear quadratic regulator embedded in the feedback linearization structure.

The actuators of the FWFR system are servomotors that have internal stable proportional-integral-derivative (PID) controllers. The internal PIDs cannot be accessed for tuning and they impose errors caused by potentiometers and clearance in gearboxes. The motion capture system in the testbed provides accurate feedback for the body control and it will be used to close the loop and override the internal PIDs of the servomotors to increase the accuracy and implement nonlinear control.

The main contribution of this work is to deliver the theoretical and experimental implementation of a nonlinear control design based on optimal feedback linearization for the extension of the manipulation range (workspace) of a flapping-wing flying robot. A claw-leg system generates this extension for the lightweight manipulator on top of the FWFR.

The rest of the paper is organized as follows. Section II presents the mathematical modeling of the system. Section III expresses the control structure. Section IV presents the simulation results. Section V presents the details of the platform and the results of the experimentation. Conclusions are expressed in Section VI.

II. Mathematical modeling

In this section, the assumptions are considered and the model is made for a maneuver after perching to increase the workspace of the robot. The contact between the claw and the branch is assumed completely elastic. The model of friction for the first joint includes three components: viscous, dynamic, and static parts. The actuation joints between the tail and body and between the body and claw are the only contributing inputs to the model for changing the pose of the ornithopter. The model studies a post-perching phase, therefore the motion of the wings is not considered as generalized coordinates in the model. The aerodynamic forces and moments generated by the movement of the tail are neglected compared to the one produced by the torque of the second joint (main actuator of the body).

Considering the robot perched on a branch, the system can be modeled as a three-degree-of-freedom manipulator, with a difference in its first joint. The first joint is passive (without an actuator) and fixed by enough friction. The friction of the first joint is due to the grasping force of the claw. The model will allow some small relative movement similar to reality when the amplitude of the moment is bigger than the friction. The other two joints are actuated by both inputs given by u_2, u_3.

In Fig. 3 a schematic view of the system is shown, where the three degrees of freedom q_i are the angles of the leg, body, and tail with respect to their local references given by the direction of the preceding arm, for $i = 1,2,3$. As stated, the first joint is passive though it moves due to the change in the dynamics and moments on the claw. It is similar to what happens in the real situation for the FWFR, and this is the reason why although q_1 is not actuated, it is considered as the first generalized coordinate. Modeling the friction is crucial to prevent the motion of the claw in simulation when the system moves. This friction modeling emulates the relative movement between the claw and the branch, based on the assumption that the first joint is passive and its angle is considered as a generalized coordinate.

Defining $\mathbf{q} = [q_1, q_2, q_3]^\top$ (rad) as the joint-angle vector and $\mathbf{u} = [0, \tau_2, \tau_3]^\top$ (Nm) as the input vector, and applying the Lagrange method, the equation-of-motion is found as a coupled system of three differential equations:

$$\mathbf{M}(\mathbf{q})\ddot{\mathbf{q}} + \mathbf{c}(\mathbf{q}, \dot{\mathbf{q}}) + \mathbf{g}(\mathbf{q}) + \mathbf{d}_\mathrm{f}(\dot{\mathbf{q}}) = \mathbf{u}, \tag{1}$$

where $\mathbf{M}(\mathbf{q}) : \mathbb{R}^3 \to \mathbb{R}^{3\times3}$ is inertia matrix, $\mathbf{c}(\mathbf{q}, \dot{\mathbf{q}}) : \mathbb{R}^3 \times \mathbb{R}^3 \to \mathbb{R}^3$ presents Coriolis and centrifugal terms and $\mathbf{g}(\mathbf{q}) : \mathbb{R}^3 \to \mathbb{R}^3$ denotes gravity vector. As already mentioned, friction is modeled as the result of the dynamic, viscous, and static components for q_1, as it can be seen in the following expression, where $\mathbf{d}_\mathrm{f} = [d_{\mathrm{f},1}, 0, 0]^\top$ is the friction vector [17]:

$$d_{\mathrm{f},1} = u_\mathrm{v}\dot{q}_1 + \frac{\dot{q}_1}{|\dot{q}_1|}\left[u_\mathrm{d} + (u_\mathrm{s} - u_\mathrm{d})\exp\left(-\frac{|\dot{q}_1|}{\varepsilon}\right)\right], \tag{2}$$

where $u_\mathrm{v}(\mathrm{kgm/s})$ represents viscous friction, $u_\mathrm{d}(\mathrm{kgm/s^2})$ indicates dynamic friction and $u_\mathrm{s}(\mathrm{kgm/s^2})$ symbolizes static friction so that the dynamic model is completed.

Moreover, introducing $\mathbf{x} = [\mathbf{q}^\top, \dot{\mathbf{q}}^\top]^\top$ as the state vector, $\dot{\mathbf{x}}$, the state-space model, is found as the first time derivative of the state-vector, and combining it with Eq. (1), the following equation is reached:

$$\dot{\mathbf{x}} = \begin{bmatrix} \dot{\mathbf{q}} \\ \mathbf{M}^{-1}(\mathbf{q})\{\mathbf{u} - \mathbf{c}(\mathbf{q}, \dot{\mathbf{q}}) - \mathbf{g}(\mathbf{q}) - \mathbf{d}_\mathrm{f}(\dot{\mathbf{q}})\} \end{bmatrix}. \tag{3}$$

III. Control Structure

An optimal feedback linearization approach has been considered for motion control and stabilization of the robot. The state-space equation of the system, Eq. (3), is considered as a nonlinear time-invariant affine-in-control system:

$$\begin{aligned} \dot{\mathbf{x}} = \mathbf{f}(\mathbf{x}) + \mathbf{g}(\mathbf{x}, \mathbf{u}) &= \mathbf{f}(\mathbf{x}) + \mathbf{B}(\mathbf{x})\mathbf{u}, \\ \mathbf{y} &= \mathbf{h}(\mathbf{x}), \end{aligned} \tag{4}$$

where $\mathbf{f}(\mathbf{x}) : \mathbb{R}^n \to \mathbb{R}^n$, $\mathbf{g}(\mathbf{x}, \mathbf{u}) : \mathbb{R}^n \times \mathbb{R}^m \to \mathbb{R}^n$ and $\mathbf{h}(\mathbf{x}) : \mathbb{R}^n \to \mathbb{R}^p$ in which n is the number of states, m is the number of inputs and p is the number of outputs. The equilibrium point of the system is $\mathbf{f}(\mathbf{0}) = \mathbf{0}$; $\mathbf{f}(\mathbf{x})$ and $\mathbf{g}(\mathbf{x}, \mathbf{u})$ are vector-valued smooth piecewise continuous functions that satisfy the Lipschitz condition. Here the measurement of the full state feedback is considered, then $p = n$. Consider the generalized coordinate vector (or a function of that) as the output variable vector, then continuous differentiation of the outputs provides [18]:

$$\mathbf{y}^{(i)} = L_f^i\mathbf{h}(\mathbf{x}) + L_g L_f^{i-1}\mathbf{h}(\mathbf{x})\mathbf{u}, \tag{5}$$

where

$$\begin{aligned} L_f^i\mathbf{h}(\mathbf{x}) &= L_f(L_f^{i-1}\mathbf{h}(\mathbf{x})) \\ &= \nabla(L_f^{i-1}\mathbf{h}(\mathbf{x}))\mathbf{f}(\mathbf{x}), \end{aligned}$$

$$\begin{aligned} L_g L_f^{i-1}\mathbf{h}(\mathbf{x}) &= L_g(L_f^{i-2}\mathbf{h}(\mathbf{x})) \\ &= \nabla(L_f^{i-2}\mathbf{h}(\mathbf{x}))\mathbf{B}(\mathbf{x}), \end{aligned}$$

in which $\nabla(\cdot) = \frac{\partial(\cdot)}{\partial \mathbf{x}}$ is Jacobian and L denotes Lie derivative. Assuming that the system is controllable, the relative degree of the system is shown by r satisfying the following condition:

$$L_g L_f^k\mathbf{h}(\mathbf{x}) = \mathbf{0}, \quad k \le r-2,$$

in the neighborhood of $\mathbf{x}_0$ and

$$L_g L_f^{r-1}\mathbf{h}(\mathbf{x}_0) \neq \mathbf{0}.$$

The control law of the feedback linearization is in the form of [18]:

$$\mathbf{u} = \frac{1}{L_g L_f^{r-1}\mathbf{h}(\mathbf{x})}(-L_f^r\mathbf{h}(\mathbf{x}) + \mathbf{v}), \tag{6}$$

where $\mathbf{v}$ is designed by linear quadratic regulator control approach. The system (4) is linearized around equilibrium point $\mathbf{x} = \mathbf{0}$ to find linearized matrices for LQR deisgn:

$$\dot{\mathbf{x}} = \mathbf{A}\mathbf{x} + \mathbf{B}\mathbf{v}, \tag{7}$$

TABLE I
THE PARAMETERS OF THE SYSTEM.

parameters	value	unit	source
m_{b}	0.4	kg	measured
m_{t}	0.05	kg	measured
m_{c}	0.17	kg	measured
$l_{\mathrm{b},1}$	0.2	m	measured
$l_{\mathrm{b},2}$	0.5	m	measured
l_{t}	0.4	m	measured
l_{c}	0.2	m	measured
I_{b}	0.016333	kgm^2	computed
I_{t}	0.00066667	kgm^2	computed
I_{c}	0.00056667	kgm^2	computed
u_{v}	20	kgm/s	estimated
u_{d}	1	$\mathrm{kgm/s}^2$	estimated
u_{s}	2.5	$\mathrm{kgm/s}^2$	estimated
ε	0.0001	–	estimated

where $\mathbf{A} \in \mathbb{R}^{n\times n}$ and $\mathbf{B} \in \mathbb{R}^{n\times m}$. The Pair of $\{\mathbf{A},\mathbf{B}\}$ is a controllable parameterization of system (4) [19]. The cost function of optimal control is defined as [20]:

$$J = \frac{1}{2}\int_0^\infty \{\mathbf{v}^\top \mathbf{R}\mathbf{v} + \mathbf{x}^\top \mathbf{Q}\mathbf{x}\}\,\mathrm{d}t, \tag{8}$$

where $\mathbf{Q} \in \mathbb{R}^{n\times n}$ and $\mathbf{R} \in \mathbb{R}^{m\times m}$ are weighting matrices of states and inputs, respectively. $\mathbf{Q}$ is symmetric positive semi-definite and $\mathbf{R}$ is symmetric positive definite. The pair of $\{\mathbf{A},\mathbf{Q}^{1/2}\}$ is a completely observable parameterization of system (4).

The control law of the LQR is [21]:

$$\mathbf{v} = -\mathbf{R}^{-1}\mathbf{B}^\top \mathbf{K}\mathbf{x}, \tag{9}$$

where $\mathbf{K} \in \mathbb{R}^{n\times n}$ is the symmetric positive definite gain of the control law, the solution to the algebraic matrix Riccati equation:

$$\mathbf{A}^\top\mathbf{K} + \mathbf{K}\mathbf{A} - \mathbf{K}\mathbf{B}\mathbf{R}^{-1}\mathbf{B}^\top\mathbf{K} + \mathbf{Q} = \mathbf{0}. \tag{10}$$

There is always a gap between the theoretical models and experimental setups due to unmodeled terms such as clearance in joints, a mismatch between the models, different distribution of inertia in the links and body of the robot with respect to the theoretical model, error in estimation and measurement of friction, etc. As a result, an integrator is augmented to the LQR to eliminate the steady-state error in the implementation. The effect of this integrator might not be seen in the simulation; however, the reduction of steady-state error in the experiment is significant due to the mismatch in the modeling process. The modified LQR plus integrator is presented as (considering error in the control law for generalizing the problem):

$$\mathbf{v}(t) = -\mathbf{R}^{-1}\mathbf{B}^\top\mathbf{K}\mathbf{e}(t) - \mathbf{K}_{\mathrm{I}}\int_0^t \mathbf{e}(\tau)\,d\tau, \tag{11}$$

where $\mathbf{e}(t) = \mathbf{x}(t) - \mathbf{x}_{\mathrm{des}}$ in which $\mathbf{x}_{\mathrm{des}}$ is the desired state vector and $\mathbf{K}_{\mathrm{I}} \in \mathbb{R}^{m\times m}$ is the integral gain, a symmetric positive definite matrix.

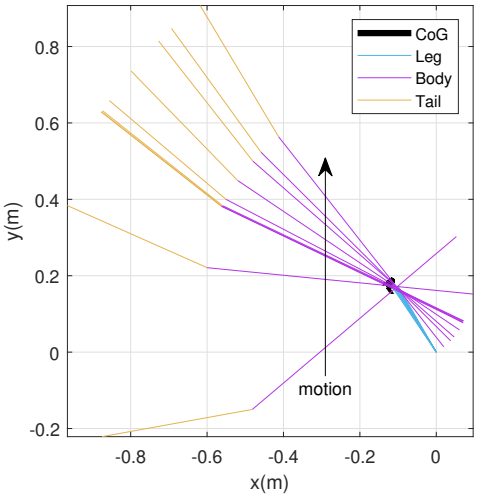

Fig. 4. The flapping-wing robot movement in the simulation.

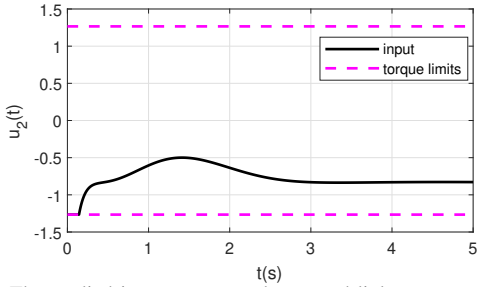

Fig. 5. The applied input torque to the second link.

IV. SIMULATION

In this section, the simulation methods that are used in solving the problem are described, as well as the analysis of the results. First, it is convenient to describe the fundamental parameters and variables that intervene in the problem. Table I shows all the physical parameters used for the simulations. The subscript "b" refers to the body, "t" to the tail, and "c" to the claw, which are the three parts of the system. The masses and the lengths were measured directly from the prototype.

Applying Eq. (6) for system (3), the following control law is obtained:

$$\mathbf{u} = \mathbf{M}(\mathbf{x})\mathbf{v} + \mathbf{c}(\mathbf{x}) + \mathbf{g}(\mathbf{x}) + \mathbf{d}_{\mathrm{f}}(\mathbf{x}), \tag{12}$$

where $u_1 = 0$ is forced to zero. Considering Table I, the linearized system matrices are also expressed:

$$\mathbf{A} = \begin{bmatrix} \mathbf{0}_{3\times3} & \mathbf{I}_{3\times3} \\ \mathbf{0}_{3\times3} & \mathbf{0}_{3\times3} \end{bmatrix}, \tag{13}$$

$$\mathbf{B} = \begin{bmatrix} 0 & 0 & 0 \\ 0 & 0 & 0 \\ 0 & 0 & 0 \\ 79.3805 & -116.3394 & 46.7217 \\ -116.3394 & 205.6453 & -169.4999 \\ 46.7217 & -169.4999 & 692.9460 \end{bmatrix}. \tag{14}$$

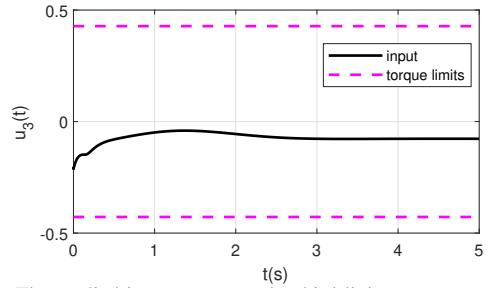

Fig. 6. The applied input torque to the third link.

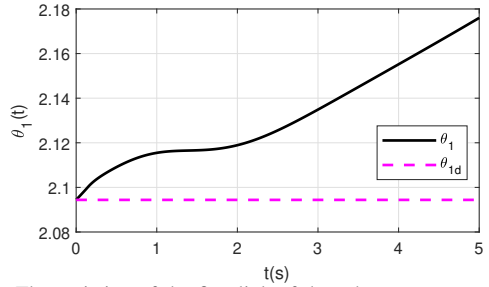

Fig. 7. The variation of the first link of the robot.

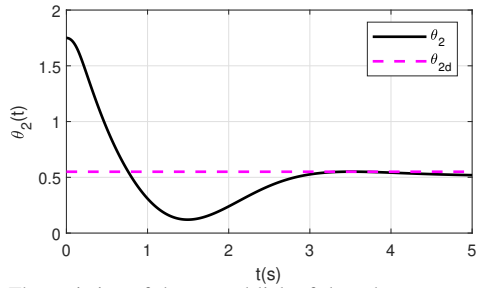

Fig. 8. The variation of the second link of the robot.

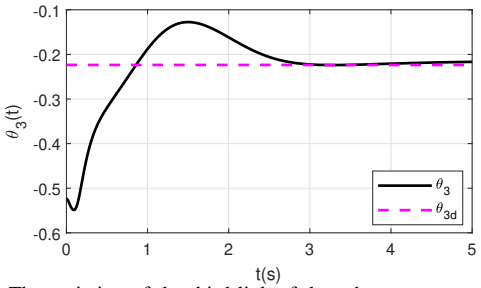

Fig. 9. The variation of the third link of the robot.

The torque limit of the motors, which are taken from the datasheet is: $\mathbf{u}_s = [0, 1.266, 0.4278]^\top$ (Nm). Considering the first passive joint, the weighting matrices are set as:

$$\mathbf{Q} = \begin{bmatrix} 1 & 0 & 0 & 0 & 0 & 0 \\ 0 & 50 & 0 & 0 & 0 & 0 \\ 0 & 0 & 50 & 0 & 0 & 0 \\ 0 & 0 & 0 & 0 & 0 & 0 \\ 0 & 0 & 0 & 0 & 10 & 0 \\ 0 & 0 & 0 & 0 & 0 & 5 \end{bmatrix}, \tag{15}$$

$$\mathbf{R} = \begin{bmatrix} 0.01 & 0 & 0 \\ 0 & 0.01 & 0 \\ 0 & 0 & 0.01 \end{bmatrix}. \tag{16}$$

Substituting (13) to (16) into algebraic Riccati equation (10), the following optimal gain is found:

$$\mathbf{K} = \begin{bmatrix} 0.1608 & 0.0183 & 0.0036 & 0.0129 & 0.0086 & 0.0012 \\ 0.0183 & 22.3721 & 0.0032 & 0.0026 & 0.0053 & 0.0010 \\ 0.0036 & 0.0032 & 15.8156 & 0.0005 & 0.0015 & 0.0013 \\ 0.0129 & 0.0026 & 0.0005 & 0.0021 & 0.0014 & 0.0002 \\ 0.0086 & 0.0053 & 0.0015 & 0.0014 & 0.0025 & 0.0005 \\ 0.0012 & 0.0010 & 0.0013 & 0.0002 & 0.0005 & 0.0004 \end{bmatrix}. \tag{17}$$

The final time of the simulation is fixed as $t_f = 5$(s), and the initial condition for position is $\mathbf{q}(0) = [2\pi/3, 1.75, -\pi/6]^\top$. The initial and final conditions of the first link have been set similarly to keep the robot steady on the branch. Final desired position is fixed as $\mathbf{q}(t_f) = \mathbf{q}(0)^\top + [0, -1.2, 0.3]^\top$. The integrator is only needed for the main body link and actuator which results in the selection of $\mathbf{K}_I$ matrix as

$$\mathbf{K}_I = \begin{bmatrix} 0 & 0 & 0 \\ 0 & 10 & 0 \\ 0 & 0 & 0 \end{bmatrix}.$$

Figure 4 shows the configuration of the robot and links between the initial and final conditions of the simulation. It can be seen that there is relatively small movement between the leg and the branch due to the realistic model of the joint (with motion and friction) explained in Section II about the physical model. It is also observed that the rest of the flapping-wing robot components moved to the desired final conditions. The magnitude of these input signals can be seen in Figs. 5 and 6, from which the conclusion is that the necessary torques to perform these movements are much lower than the available stall torques of motors. The exerted torque corresponding to the first degree of freedom is not shown because, as explained above, it does not have an actuator; the claw of the flapping-wing robot attached to the branch, where we find a certain relative movement that is not due to the action of a motor, but for the reaction to the motion of the body and tail. Figures 7-12 show the temporal evolution of the three degrees of freedom and their corresponding angular velocities during the simulation. It is observed that the relative movement between the branch and the leg is, in magnitude of the order, lower than the movements of the body and the tail. The speeds of the body and the tail tend to zero, stabilizing the system to be able to manipulate once the desired position conditions are reached. It is observed that the angular velocity between the branch and the leg does not reach exactly zero. This is because this degree of freedom has been modeled as a movement (of small magnitude), which presents small changes, but in reality, it is not entirely true, it actually would be a movement that ends up stopping. Although the desired final position is indeed reached, the obtained error is acceptable. Lastly, it is worth mentioning that, as can be seen in Fig. 4, the

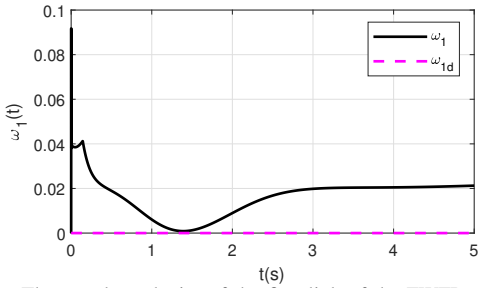

Fig. 10. The angular velocity of the first link of the FWFR.

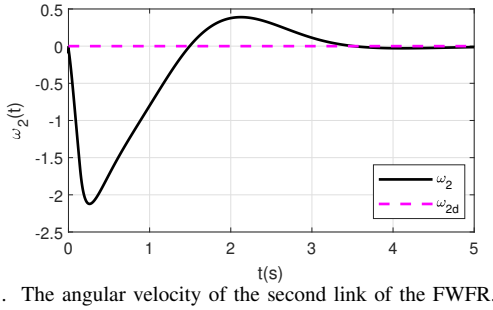

Fig. 11. The angular velocity of the second link of the FWFR.

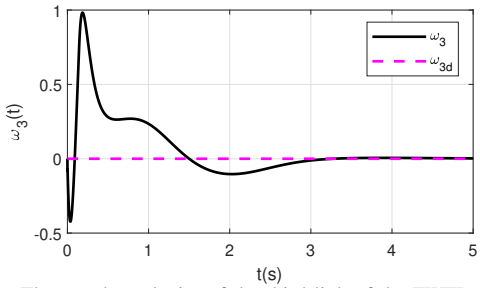

Fig. 12. The angular velocity of the third link of the FWFR.

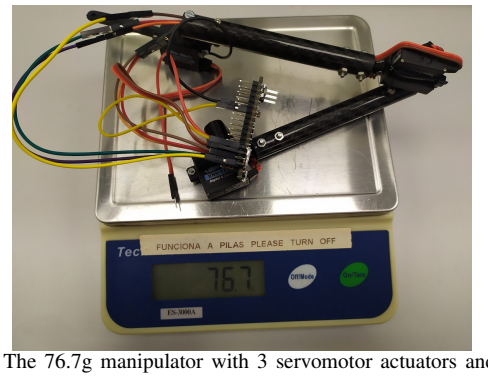

Fig. 13. The 76.7g manipulator with 3 servomotor actuators and Arduino Micro processing board.

system movement achieves the goal of this study, which is to substantially change the space work for manipulation.

V. Experimental Platform and Results

A manipulation operation after perching needs a stable platform as the base of the system. It should resist and hold its position on the branch and hold the robot steady on it while the manipulator is moving. Due to the size limitation, the manipulator generates a workspace of 20(cm) in length while the arm is stretched. So, the leg also could be used as a tool to extend the workspace as expressed in the introduction. Here as a preliminary work of the body control after perching, experimental validation of the feedback linearization with linear quadratic regulator and integral effect has been implemented on a real prototype.

The manipulator is a two-degree-of-freedom arm, planar in XZ plane while gravity is in Z direction. The links of the arm are 12(mm)-diameter carbon-fiber tubes and the actuators are lightweight BMS-115HV Blue Bird servomotors, 11.3(g) each one, producing 5.5(kg.cm) torque at 7.4(V). The total weight of the system considering a simple 3D printed gripper and Arduino Micro processing board was gained 76.7(g), presented in Fig. 13. The flapping-wing flying robot, as the target platform for carrying the manipulator, is the high-payload E-Flap prototype [22], modified with an active leg designed for perching [1]. The leg facilitates the body control after perching thanks to its high torque 18.5(kg.cm), generated by low weight 34(g) servomotor, while its energy-storing claw embraces the branch with maximum grip after impact and releases the pre-stored energy for grasping.

The purpose of these experimental tests is to ensure that the feedback linearization (with LQR) controller regulates the system to the desired output, as well as to verify its robustness when modeling errors occur. The servomotors have internal closed-loop controllers with potentiometer feedback. This reduces the precision of the system and motivated us to close the loop with an outer loop controller with Opti-Track external vision feedback. The Opti-Track system generates motion capture visual position and orientation feedback of the robot with 100(Hz) by installing markers on the robot.

The manipulator is located at the head of the E-Flap to have the maximum reachability of the system for manipulation tasks. In order to keep the shift in the center of mass of the robot at a minimum level, the arm will spread over the body during the flight. This concept was investigated and flight capability was demonstrated in Ref. [4].

The self-programmed controller board consists of a Nanopi Neo Air with a Quad-core Allwinner H3 processor, where the nonlinear controller and a kinematic model of the servomotors have been implemented following the control diagram in Fig. 14. To compensate for the unknown servomotor behavior, a linear mapping of torque to the position was regarded to adjust the LQR output to the servomotors input. As the LQR + Integrator is more robust than FL (presented in Section III, Eq. (11)), it should handle the uncertainty between the modeling and experimental platform.

Test without manipulator for validation of the controller. As a first stage of the experiment, the controller was tested on the F-flap without the manipulator, to validate the controller. Figure 15 illustrates how the initial approach to the setpoint is divided by the effect of the FL+LQR (fast) response and then the integrator (slow) provides a high accuracy correction

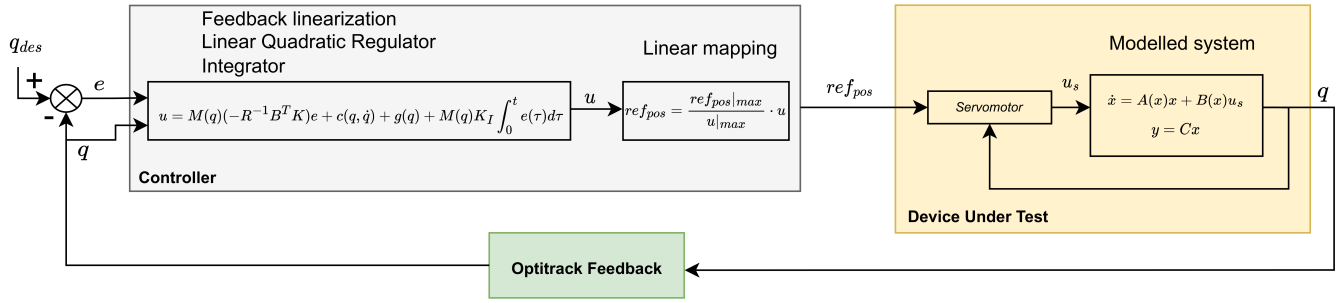

Fig. 14. The control diagram of the practical implementation of feedback linearization plus LQR and integrator design.

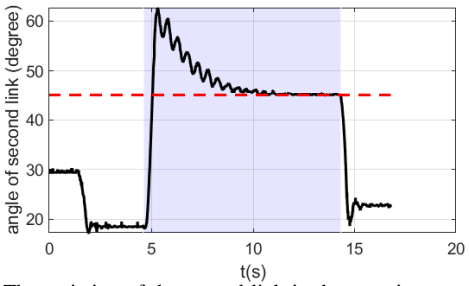

Fig. 15. The variation of the second link in the experiment, setpoint 45°.

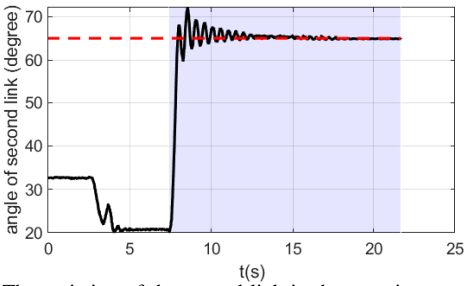

Fig. 17. The variation of the second link in the experiment, setpoint 65°.

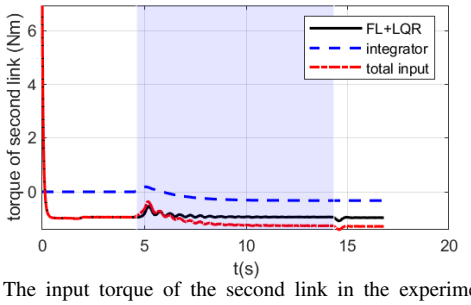

Fig. 16. The input torque of the second link in the experiment, and its components, main signal, and integrator, setpoint 45°.

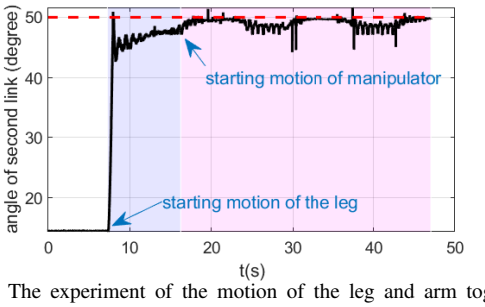

Fig. 18. The experiment of the motion of the leg and arm together and the performance of the controller on keeping the robot steady in the desired position.

with oscillations once close to the desired setpoint. A control signal breakdown is shown in Fig. 16, where we can see how the LQR gives the quick input to move the system to the operating point while the integrator provides the controller with zero steady-state error. The necessity of an integrator was already expected and presented in the mathematical modeling Eq. (11), due to the uncertainty in the modeling and the unknown behavior of the servomotor (which has an internal inaccessible controller). Considering a higher second link reference, as shown in Fig. 17, the initial response due to the linear mapping is similar, but the transition towards zero steady-state error is faster.

Final test with the integrated manipulator. The second stage in experiments was to validate the performance of the controller while the manipulator moves and imposes disturbance to the controlled system. In Fig. 18 the variation of the body, the second link, is plotted in time, the light blue zone covers the motion of the leg and the light pink zone presents the motion of the manipulator while the leg regulates the system to the desired point and tries to keep the system steady on the branch. As we considered a fast response LQR and an integrator for regulation towards zero steady-state error, the error did not reach zero during the transition of the manipulator, but the error was minimized and the leg tried to compensate for the disturbance. The controller reaction to manipulator oscillations was presented in Fig. 19.

VI. Conclusion

This paper investigated the modeling and control of a flapping-wing robot, perched on a branch to increase the workspace of the manipulator using the active leg-claw system. The leg-claw system was attached to the branch and provides enough friction to keep the bird steadily on that. Modeling was done including the motion of the leg to present a realistic scenario for the control and simulation. Therefore,

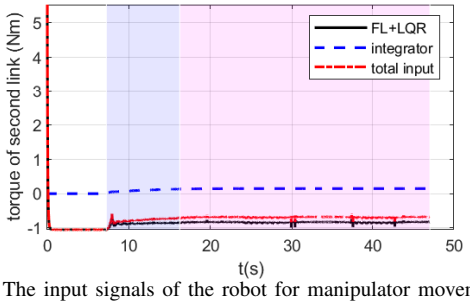

Fig. 19. The input signals of the robot for manipulator movement experiment.

a small variation was observable in the simulation for the first joint (leg). A feedback linearization has been designed for controlling the system. A linear quadratic regulator was embedded in the control to add optimality to the system and easy tuning of the linear controller of the FL. The simulation showed that the controlled leg increased (shifted) the workspace drastically and the results also demonstrated the extension of the workspace. The kinematics transformation between the joint angles and end-effectors could be incorporated into the dynamics and treated by output-feedback-based controllers [23]–[25], to command in Cartesian coordinates which is proposed for future studies.

VII. Acknowledgement

This work was supported by the GRIFFIN ERC Advanced Grant 2017, Action 788247; and partial support by PAIDI 2020 through the Project HOMPOT under Grant P20_00597.

References

[1] R. Zufferey, J. Tormo-Barbero, D. Feliu-Talegón, S. R. Nekoo, J. Á. Acosta, and A. Ollero, "How ornithopters can perch autonomously on a branch," *Nature Communications*, vol. 13, no. 1, pp. 1–11, 2022.

[2] D. Feliu-Talegon, J. Á. Acosta, A. Suarez, and A. Ollero, "A bio-inspired manipulator with claw prototype for winged aerial robots: Benchmark for design and control," *Applied Sciences*, vol. 10, no. 18, p. 6516, 2020.

[3] D. Feliu-Talegon, J. Á. Acosta, and A. Ollero, "Control aware of limitations of manipulators with claw for aerial robots imitating bird's skeleton," *IEEE Robotics and Automation Letters*, vol. 6, no. 4, pp. 6426–6433, 2021.

[4] S. R. Nekoo, D. Feliu-Talegon, J. A. Acosta, and A. Ollero, "A 79.7 g manipulator prototype for e-flap robot: A plucking-leaf application," *IEEE Access*, vol. 10, pp. 65300–65308, 2022.

[5] W. R. Roderick, M. R. Cutkosky, and D. Lentink, "Bird-inspired dynamic grasping and perching in arboreal environments," *Science Robotics*, vol. 6, no. 61, p. eabj7562, 2021.

[6] T.-J. Lin, S. Long, and K. A. Stol, "Automated perching of a multirotor uav atop round timber posts," in *2018 IEEE/ASME International Conference on Advanced Intelligent Mechatronics (AIM)*, pp. 486–491, IEEE, 2018.

[7] W. Stewart, L. Guarino, Y. Piskarev, and D. Floreano, "Passive perching with energy storage for winged aerial robots," *Advanced Intelligent Systems*, p. 2100150, 2021.

[8] W. Stewart, E. Ajanic, M. Müller, and D. Floreano, "How to swoop and grasp like a bird with a passive claw for a high-speed grasping," *IEEE/ASME Transactions on Mechatronics*, 2022.

[9] K. C. Broers and S. F. Armanini, "Design and testing of a bioinspired lightweight perching mechanism for flapping-wing mavs using soft grippers," *IEEE Robotics and Automation Letters*, 2022.

[10] A. E. Gomez-Tamm, V. Perez-Sanchez, B. C. Arrue, and A. Ollero, "Sma actuated low-weight bio-inspired claws for grasping and perching using flapping wing aerial systems," in *2020 IEEE/RSJ International Conference on Intelligent Robots and Systems (IROS)*, pp. 8807–8814, IEEE, 2020.

[11] C. A. Laubscher, A. Goo, R. J. Farris, and J. T. Sawicki, "Hybrid impedance-sliding mode switching control of the indego explorer lower-limb exoskeleton in able-bodied walking," *Journal of Intelligent & Robotic Systems*, vol. 104, no. 4, pp. 1–14, 2022.

[12] J.-J. Zhang, Z.-L. Fang, Z.-Q. Zhang, R.-Z. Gao, and S.-B. Zhang, "Trajectory tracking control of nonholonomic wheeled mobile robots using model predictive control subjected to lyapunov-based input constraints," *International Journal of Control, Automation and Systems*, vol. 20, no. 5, pp. 1640–1651, 2022.

[13] A. Perrusquía, "Robust state/output feedback linearization of direct drive robot manipulators: A controllability and observability analysis," *European Journal of Control*, vol. 64, p. 100612, 2022.

[14] V. Bahrami, A. Kalhor, and M. Tale Masouleh, "Dynamic modeling and design of controller for the 2-dof serial chain actuated by a cable-driven robot based on feedback linearization," *Proceedings of the Institution of Mechanical Engineers, Part C: Journal of Mechanical Engineering Science*, vol. 236, no. 5, pp. 2546–2558, 2022.

[15] L. Martins, C. Cardeira, and P. Oliveira, "Feedback linearization with zero dynamics stabilization for quadrotor control," *Journal of Intelligent & Robotic Systems*, vol. 101, no. 1, pp. 1–17, 2021.

[16] M. H. Korayem, M. Yousefzadeh, and H. Tourajizadeh, "Optimal control of a wheeled mobile cable-driven parallel robot icasbot with viscoelastic cables," *Robotica*, vol. 38, no. 8, pp. 1513–1537, 2020.

[17] R. J. Schilling, *Fundamentals of robotics: analysis and control*. Simon & Schuster Trade, 1996.

[18] J.-J. E. Slotine, W. Li, *et al.*, *Applied nonlinear control*, vol. 199. Prentice hall Englewood Cliffs, NJ, 1991.

[19] V. L. Mehrmann, *The autonomous linear quadratic control problem: theory and numerical solution*. Springer, 1991.

[20] D. E. Kirk, *Optimal control theory: an introduction*. Courier Corporation, 2004.

[21] S. Kazemi and S. Rafee Nekoo, "Robust finite-time feedback linearization control of robots: theory and experiment," *Journal of the Brazilian Society of Mechanical Sciences and Engineering*, vol. 40, no. 8, pp. 1–11, 2018.

[22] R. Zufferey, J. Tormo-Barbero, M. M. Guzmán, F. J. Maldonado, E. Sanchez-Laulhe, P. Grau, M. Pérez, J. Á. Acosta, and A. Ollero, "Design of the high-payload flapping wing robot e-flap," *IEEE Robotics and Automation Letters*, vol. 6, no. 2, pp. 3097–3104, 2021.

[23] S. R. Nekoo, "Output-and state-dependent riccati equation: An output feedback controller design," *Aerospace Science and Technology*, p. 107649, 2022.

[24] K. Shojaei and H. Taghavifar, "Input-output feedback linearization control of a tractor with n-trailers mechanism considering the path curvature," *Proceedings of the Institution of Mechanical Engineers, Part C: Journal of Mechanical Engineering Science*, vol. 236, no. 17, pp. 9700–9715, 2022.

[25] N. Rao and S. Sundaram, "An input-output feedback linearization based exponentially stable controller for multi-uav payload transport," *arXiv preprint arXiv:2207.04375*, 2022.